Direct numerical simulation of hydrogen addition in turbulent premixed Bunsen flames using flamelet generated manifold reduction

January, 2009

A.W. Vreman[1,2], J.A. van Oijen[1], L.P.H. de Goey[1] and R.J.M. Bastiaans[1,3]

[1] Combustion Technology, Department of Mechanical Engineering, Technische Universiteit Eindhoven, Den Dolech 2, 5600 MB Eindhoven, The Netherlands

[2] Vreman Research, Godfried Bomansstraat 46, 7552 NT Hengelo The Netherlands

Preprint; published in Int. J. Hydrogen Energy 34, 2778-2788 (2009).

[3]Author to whom correspondence should be addressed; electronic mail: r.j.m.bastiaans@tue.nl.

Abstract
Direct numerical simulations of a lean premixed turbulent Bunsen flame with hydrogen addition have been performed. We show results for a case with equivalence ratio 0.7 and a molar fractional distribution of 40% H_2 and 60% CH_4. The flamelet generated manifold technique is used to reduce the chemistry; flamelets with different equivalence ratio and inflow temperature are used to account for stretch effects induced by preferential diffusion. The three-dimensional simulation clearly shows enhanced burning velocity in regions convex toward the reactants and reduced burning velocity with possible extinction in regions concave toward the reactants. To obtain these effects it was found to be necessary to include two three-dimensional transport equations with essentially different diffusivities. This point is illustrated by comparison of the results with cases in which either a single transport equations was used or two transport equations with minor differences in diffusivities were used. These latter cases incorporated preferential diffusion in the 1D flamelets, but not in 3D. Thus the 3D preferential diffusion effects are shown to enhance curvature and thereby to increase the turbulent burning velocity and reduce the mean flame height. In addition the turbulent burning velocity increases because hydrogen addition leads to a larger laminar flamelet consumption speed. To demonstrate this second effect, results of the cases mentioned above are compared to results of simulations of the Bunsen flame simulations with 0% hydrogen added to the fuel.

1 Introduction

Turbulent methane-air flames are probably the most extensively studied turbulent flames. Hydrogengen-air turbulent combustion has also received considerable attention [1, 2, 3, 4, 5]. For turbulent flames with hydrogen added to methane the literature is more limited; we mention the experimental studies reported in Refs. [6, 7, 8, 9] and the two-dimensional DNS (with a chemical mechanism reduced to 19 species and 15 reactions) by Hawkes & Chen [10]. The topic of hydrogen addition has become important recently, in particular because of the need to increase the knowledge about the effects of biomass addition to regular fuels. Hydrogengen addition in laminar flames has been studied more than in turbulent flames; it is well-known that the addition of hydrogen increases the laminar burning velocity of a one-dimensional lean premixed methane-air flame considerably [11, 12, 13, 14, 15, 16].

In this paper we consider the effect of adding hydrogen to a premixed turbulent methane-air flame, by means of three-dimensional direct numerical simulation. The flame is a turbulent Bunsen flame where the lean fuel, which contains both methane and hydrogen, is ejected through a small rectangular slot. The flow configuration is similar to experiments performed for methane fuel by Filatyev *et al.* [17] and simulations by Bell *et al.* [18] and Sankaran *et al.* [19]. The size of the flame is somewhat smaller in our case, to enable well-resolved Direct Numerical Simulation (DNS) with moderate computational effort. Both flame thickness and turbulence are resolved down to the Kolmogorov length-scale.

To resolve all relevant scales with acceptable computational effort, we introduce a suitable flamelet parametrization of the chemistry, such that only few scalar transport equations are needed to carry the chemistry in 3D. The flamelet method utilizes a parametrization of the local flame chemistry based on one-dimensional laminar flames [20]. Since flamelets are one-dimensional, they can be solved using detailed chemistry reaction mechanisms. For methane, we performed DNS of Bunsen flames with flamelet chemistry before [21, 22].

The flamelet method in the present paper is an extension of earlier premixed flamelet methods, for example the so-called flamelet generated manifold technique (FGM), which is basically a mapping of the entire premixed chemistry upon the progress variable [23, 24, 25]. The flamelets in a flamelet method are usually computed with a detailed chemistry reaction scheme, which in our case is GRI 3.0, which involves 53 transport equations and more than 300 chemical reactions [26]. An extension of standard flamelet methods is needed when we consider hydrogen addition to the methane, within the setting of lean combustion (equivalence ratio $\phi = 0.7$). Since the Lewis number of hydrogen is low, preferential diffusion becomes important when hydrogen is added. Preferential diffusion causes so-called thermo-diffusive instabilities [27]. Because of the large diffusion of hydrogen a relative large amount of fuel is transported to regions that are convex toward the unburnt mixture. This implies a local increase of the equivalence ratio and thus a local increase of the burning velocity in these regions.

In this work we will focus on the case where the contribution of hydrogen to the sum of methane and hydrogen in the fuel equals 40% (molar percentage). We will distinguish between two sets of simulations. Set I corresponds to a Bunsen flame with slot width 8mm. The effect of preferential diffusion in this case will be addressed by comparing results of two flamelet simulations: simulation A40, in which preferential diffusion was

included in the 3D transport equations, and simulation B40, in which preferential diffusion was discarded in the 3D transport equations. To contrast the results with results for 0% hydrogen addition, simulations for smaller slot width (4mm) had to be performed (simulation set II). Into these simulations various choices for the control variables that span the manifold were included, and we will show the resulting differences with 0% H_2 and investigate the influence of the weight factor of the mass fraction H_2 in the progress variable.

The structure of the paper is as follows. We will present the flamelet method and the governing equations in section 2. In section 3 we will continue with the description of the problem, by specifying the Bunsen flow configuration and the numerics. Also the set of simulations for the larger slot width will be defined there. Results of that set will be shown in section 4. In section 5 we will define the simulations for the smaller slot width and show the corresponding results. Finally, the conclusions will be summarized in section 5.

2 Governing equations

In order to perform well-resolved DNS with moderate computational effort, the flamelet-generated manifold (FGM) method is applied [24]. In this approach, laminar flamelets are computed with a detailed reaction model and the solutions are stored in a lookup table. The most elementary version is a 1D FGM, which is constructed from a single premixed flamelet and can be parameterized by a single control variable. Since the enthalpy and the mass fractions of the elements are conserved in such a flamelet, a 1D FGM cannot account for changes in these variables, which arise due to the combined effect of preferential diffusion and stretch [29]. In [30] it was shown how these effects can be included in the FGM approach for methane-air flames. In principle, for each quantity that is conserved by chemical reactions but changes due to stretch effects (i.e. enthalpy and element mass fractions), an additional dimension has to be added to the manifold. This means that the 1D manifold should be extended to a $N_e + 1$ dimensional manifold, with N_e the number of elements. Because this is unwanted from a computational point of view, the number of dimensions is reduced by assuming a relation between the changes in enthalpy and element mass fractions. In [30] a linear relation between the changes in these variables was derived for weakly stretched flames. It was shown that a 2D FGM could be constructed using this relation and that the effect of preferential diffusion and stretch on the mass burning rate could be predicted by this manifold.

A more convenient way to generate a 2D manifold is to compute flamelets for a range of equivalence ratios ϕ. In [3, 25], this approach is used to construct a 2D manifold for stretched hydrogen-air flames. This approach is however less accurate because it wrongfully assumes that the changes in elements and enthalpy corresponds to a change in ϕ only. Recently, it has been shown in [31] that the equivalence ratio by itself is not enough, but that the combined effect of equivalence ratio and temperature can describe the main effects of stretch and preferential diffusion on the mass burning rate of methane-hydrogen-air flames. Therefore, a 2D manifold is constructed here by changing the equivalence ratio ϕ and the temperature T_0 of the unburnt mixture simultaneously. The ratio between the changes $\Delta\phi/\Delta T_0$ is determined from the changes in enthalpy Δh and element mass fractions ΔZ_j in a stretched flame. Since the derivatives $\partial Z_j/\partial\phi$,

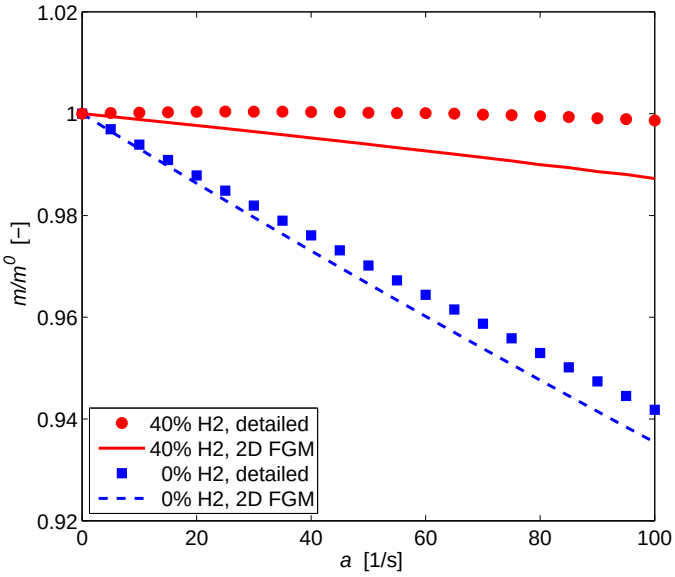

Figure 1: Normalized mass burning rate m/m^0 as function of strain rate a for $\psi = 0$ (•) and $\psi = 0.4$ (■). Comparison between FGM (lines) and detailed simulation (symbols) of one-dimensional stretched laminar premixed counterflow flames.

$\partial h/\partial\phi$, $\partial Z_j/\partial T_0$ and $\partial h/\partial T_0$ are known, the changes $\Delta\phi$ and ΔT_0 can be found by solving the overdetermined system (N_e equations and two unknowns)

$$\begin{bmatrix} \partial h/\partial\phi & \partial h/\partial T_0 \\ \partial Z_1/\partial\phi & \partial Z_1/\partial T_0 \\ \vdots & \vdots \\ \partial Z_{N_e-1}/\partial\phi & \partial Z_{N_e-1}/\partial T_0 \end{bmatrix} \begin{bmatrix} \Delta\phi \\ \Delta T_0 \end{bmatrix} = \begin{bmatrix} \Delta h \\ \Delta Z_1 \\ \vdots \\ \Delta Z_{N_e-1} \end{bmatrix} \tag{1}$$

in a least squares fashion. For the H_2 fuel fraction $\psi = 0.4$ with equivalence ratio $\phi = 0.7$, this results in $\Delta\phi/\Delta T_0 = 0.6 \times 10^{-3}\,\mathrm{K}^{-1}$. Based upon this ratio, flamelets were computed between $T_0 = 250\,\mathrm{K}$ ($\phi = 0.67$) and $T_0 = 400\,\mathrm{K}$ ($\phi = 0.76$) with $\Delta T_0 = 2\,\mathrm{K}$. Diffusion was governed by constant Lewis numbers Le_i. For example, the Lewis numbers of the two species CH_4 and H_2 (labeled as species 1 and 2 respectively) were $Le_1 = 0.99$ and $Le_2 = 0.30$.

The 2D FGM has been validated against detailed simulations of one-dimensional stretched counterflow flames. In Fig. 1 the normalized mass burning rate of these flames is shown as function of strain rate a. The results for the 0% hydrogen case are also included. The figure shows that the mass burning rate of stretched flames is indeed predicted quite satisfactorily by a manifold based upon variations of T_0 and ϕ as described above.

Next we continue with a description of the manifold for $\psi = 0.4$. Since the variations of T_0 and ϕ are coupled, the flamelets form a two-dimensional space. Therefore the manifold should be parameterized by two control variables, for which we select a progress variable c and the temperature T. The progress variable should vary monotonically with respect to the spatial flamelet coordinate and represent the burning of both species in the fuel

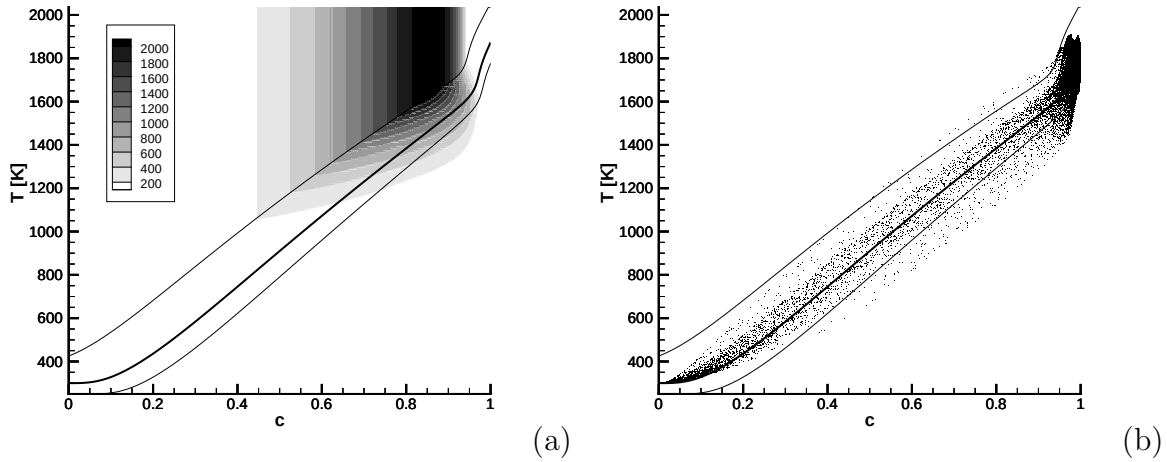

Figure 2: Manifold A40 (a) with contours of source term ω_c [kg/(m^{3}s)]. The thick solid curve corresponds to the basic flamelet ($\phi = 0.70$, $T_0 = 300$K). The lower thin solid curve represents the outer flamelet $\phi = 0.67$ ($T_0 = 250$K), and the upper thin solid curve the outer flamelet $\phi = 0.76$ ($T_0 = 400$K). The scatter plot (b) shows actual (c, T) combinations that were accessed by simulation A40a (defined later on).

(CH_4 and H_2). These conditions are satisfied when the progress variable c is defined by:

$$c = 1 - \frac{Y}{Y_{max}}, \tag{2}$$

where

$$Y = \frac{Y_1}{M_1} + \frac{Y_2}{M_2}, \tag{3}$$

and Y_{max} is based on the maximum value of Y for the basic flamelet ($T_0 = 300\,\mathrm{K}$). The symbols Y_i and M_i denote mass fraction and molar weight of species i, respectively.

The resulting manifold is shown in Fig. 2, including a contour plot of the chemical source term of the progress variable,

$$\omega_c = -(\frac{\omega_1}{M_1} + \frac{\omega_2}{M_2})/Y_{max}, \tag{4}$$

where ω_i equals the source-term of species i evaluated from the flamelets. The c and T directions were discretized with 200 uniform intervals each. The basic flamelet (thick curve), and the outer flamelets $\phi = 0.67$ (lowest thin curve) and $\phi = 0.76$ (highest thin curve) are also shown. Between the thin curves the manifold was obtained from linear interpolation between flamelets, while outside these curves suitable extrapolation was used. Above the curve $\phi = 0.76$ constant extrapolation in vertical direction was used; this region was seldom used by the simulations in this paper. However, the region below the curve $\phi = 0.67$ was accessed more frequently (see the scatter points drawn in Fig. 2). Therefore a more sophisticated extrapolation was used in that region, resulting in a natural extension of the manifold below the curve $\phi = 0.67$ (see Fig. 2). However, we found that details of the extrapolation were not important (see section 4): constant extrapolation in the vertical direction provided the same statistical numbers for turbulent

burning velocity and mean flame height (within 1%). We also verified that representation of the lower region by additional flamelets instead of extrapolation did not alter the results either.

Next we specify the equations that were solved in 3D:

$$\frac{\partial \rho}{\partial t} + \frac{\partial \rho u_j}{\partial x_j} = 0, \tag{5}$$

$$\frac{\partial \rho u_i}{\partial t} + \frac{\partial \rho u_i u_j}{\partial x_j} = -\frac{\partial p}{\partial x_i} + 2\frac{\partial \mu S_{ij}}{\partial x_j}, \tag{6}$$

$$\frac{\partial \rho c_P T}{\partial t} + \frac{\partial \rho c_P u_j T}{\partial x_j} = \frac{\partial}{\partial x_j}\Big(\rho c_P D \frac{\partial T}{\partial x_j}\Big) + \zeta + \omega_T, \tag{7}$$

$$\frac{\partial \rho c}{\partial t} + \frac{\partial \rho u_j c}{\partial x_j} = \frac{\partial}{\partial x_j}\Big[\frac{\rho D}{Y_{max}}\Big(\frac{1}{M_1 Le_1}\ \frac{\partial Y_1}{\partial x_j} + \frac{1}{M_2 Le_2}\ \frac{\partial Y_2}{\partial x_j}\Big)\Big] + \omega_c, \tag{8}$$

$$\frac{\partial \rho Y_3}{\partial t} + \frac{\partial \rho u_j Y_3}{\partial x_j} = \frac{\partial}{\partial x_j}\Big(\frac{\rho D}{Le_3}\ \frac{\partial Y_3}{\partial x_j}\Big) + \omega_3, \tag{9}$$

where the summation convention over repeated indices is used, while ρ, $\mathbf{u}$, p, T represent density, velocity vector, pressure, temperature, while

$$\mu = 1.72 \cdot 10^{-5} (T/298\ \mathrm{K})^{0.521}\ \mathrm{kg/(ms)}, \tag{10}$$

$$\rho D = 2.71 \cdot 10^{-5} (T/298\ \mathrm{K})^{0.673}\ \mathrm{kg/(ms)}, \tag{11}$$

$$S_{ij} = \tfrac{1}{2}\Big(\frac{\partial u_i}{\partial x_j} + \frac{\partial u_j}{\partial x_i} - \frac{2}{3}\frac{\partial u_k}{\partial x_k}\delta_{ij}\Big), \tag{12}$$

are viscosity, diffusivity [32], and strain-rate respectively. The equation for c results from the summation of the equations for Y_1 and Y_2 and the definitions of c and ω_c.

A number of quantities were read from the flamelet database. All these quantities depended on the variables c and T. The quantities read from the database were: density ρ, fuel species Y_1 and Y_2, source-term ω_c in the progress variable equation, c_P, ζ, heat-release term ω_T in the temperature equation, and source-term ω_3 in the equation for the mass fraction of NO (Y_3). The latter transport equation is passive. Since the increase of the mass fraction of NO is a relatively slow process, an additional transport equation is able to provide much more accurate results than direct evaluation of the mass fraction of NO from the manifold [33]. The quantity ζ contains the gradients of all species,

$$\zeta = \sum_i \frac{\rho c_{P,i} D}{Le_i} \frac{\partial Y_i}{\partial x_k}\ \frac{\partial T}{\partial x_k}. \tag{13}$$

This quantity was evaluated in one-dimension for each flamelet and then stored in the table.

The progress variable equation (8) incorporates effects of the low Lewis number of H_2 by the nontrivial expression for diffusion. The diffusion term is not standard since the three dimensional gradients inside are not proportional to the gradient of c only. Since Y_1 and Y_2 are functions of c and T, differentiation shows that, mathematically, the diffusion flux is proportional to a linear combination of the gradient of c and the gradient of T. An alternative expression of the diffusion term in the equation for c will be introduced in section 4.

Case	h [mm]	grid	variation
A40	0.1	$160 \times 256 \times 320$	
A40a	0.1	$160 \times 256 \times 320$	constant extrapolation
A40b	0.1	$160 \times 256 \times 320$	101 flamelets
A40c	0.2	$160 \times 256 \times 320$	ζ omitted
B40	0.1	$160 \times 256 \times 384$	

Table 1: Overview of simulations of turbulent Bunsen flame with slot width 8mm. The first symbols in the name of the case denotes the manifold that is used. The term ζ is included and the sophisticated manifold extrapolation based upon 76 flamelets is applied unless indicated otherwise.

By solving the equation for T simultaneously with the equation for c (that reflects effects of the low Lewis number of H_2), three-dimensional dynamic effects of preferential diffusion were incorporated. The corresponding two-dimensional manifold for 40% H_2 was labeled manifold A40. To investigate the effect of preferential diffusion this manifold was simplified to a one-dimensional manifold B40, represented by the basic flamelet only (thick curve in Fig. 2). For simulations with manifold B40, the temperature equation was switched off. Instead the temperature T became a function of c only; it was stored into and read from the database.

3 Flame configuration, numerics and definition of simulation set I

The planar Bunsen flame simulated was composed of a central jet with maximum mean velocity of $u_0 = 3$m/s, through a slot with width 8mm. The inflow temperature of the jet was 300K, and the inflow composition of the jet is a lean methane-air mixture mixed with hydrogen. The reactant jet was surrounded by a hot co-flow of 7m/s. The molar fraction of hydrogen (ψ) equalled 0.4. Since the molar weight of H_2 is very low, the inlet mass flux and the input of chemical energy were hardly changed compared to $\psi = 0$. The equivalence ratio of the fuel equalled 0.7. The numerical method has been extensively described and tested in Refs. [21, 22]. Basically second-order accurate finite differences were used, and a Poisson equation was solved to obtain the pressure.

An overview of the simulations performed is shown in Table 1. The grid size was 0.1mm in each case; cells were cubical and uniform. Momentum and Poisson equation were integrated at each basic time-step ($1.6 \cdot 10^{-6}$s), but the T, c and NO equations were integrated at two substeps for the simulations listed in table 1. Substeps were introduced to handle the stability restriction imposed by the diffusion term of c more efficiently; without substeps a smaller basic time-step would have been necessary. With the present choices overshoots of c remained below 1.0003. The boundary conditions were inflow and outflow in the streamwise direction (z), outflow in the normal direction (y), and periodicity in spanwise direction (x).

The mean inflow was prescribed by the basic flamelet profiles in physical space for the temperature and progress variable, where $T = 1504$K was positioned at $y = \pm 4$mm.

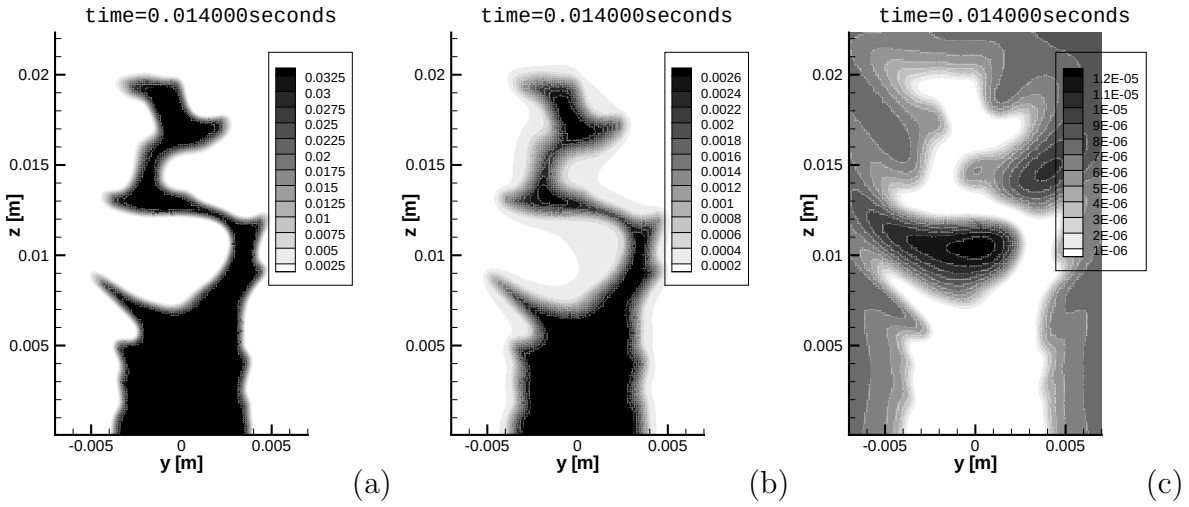

Figure 3: Contours of instantaneous fields in the vertical plane $x_1 = 0$mm, for simulation A40 with 2D manifold: mass fraction of CH_4 (a), mass fraction of H_2 (b), and mass fraction of NO (c).

This implied that, in the inflow plane, the progress variable level $c = 0.5$ occurred at $y = \pm 3.8$mm. The corresponding locations of the maximum source term of the progress variable were at $y = \pm 4.0$mm. The thermal thickness of the basic flamelet (based on maximum temperature gradient) was approximately 0.53mm. As mean inflow, velocity tangent hyperbolic functions with the maximum shear regions located at $y = \pm 4$mm were used for u_z (thickness 0.384mm, based upon maximum velocity gradient), while the means of the other velocity components were zero. Perturbations were added to the three inflow velocity components, mimicking grid turbulence at the inflow with an intensity of 0.65m/s, Kolmogorov length of 0.1mm and $Re_\lambda \approx 50$. The inflow turbulence was restricted to $|y| \leq 4$mm. For details about the procedure that generated the inflow turbulence we refer to Refs. [21, 22].

4 Results of simulation set I

In this section we discuss three types of results: snapshots of important chemical species for case A40, a comparison between A40 and B40 to show the effect of preferential diffusion on the turbulent flame, and finally mean statistical numbers for all simulations performed for the slot width of 8mm.

Figure 3 gives an impression of the shape of the flame in a two-dimensional plane at certain time. The mass fractions of CH_4, H_2 and NO are shown. The first two species form the basis for the progress variable, and thus the flame front is represented by the thin region where these quantities vary. Compared to CH_4, the variation of H_2 is clearly smoother, which is caused by the low Lewis number and therefore relatively large molecular diffusion of H_2. Important variations of NO occur at the burnt side of the flame front, illustrating the relatively slow process of NO formation. The maximum value of NO is small (only $1.2 \cdot 10^{-5}$), because the combustion is lean.

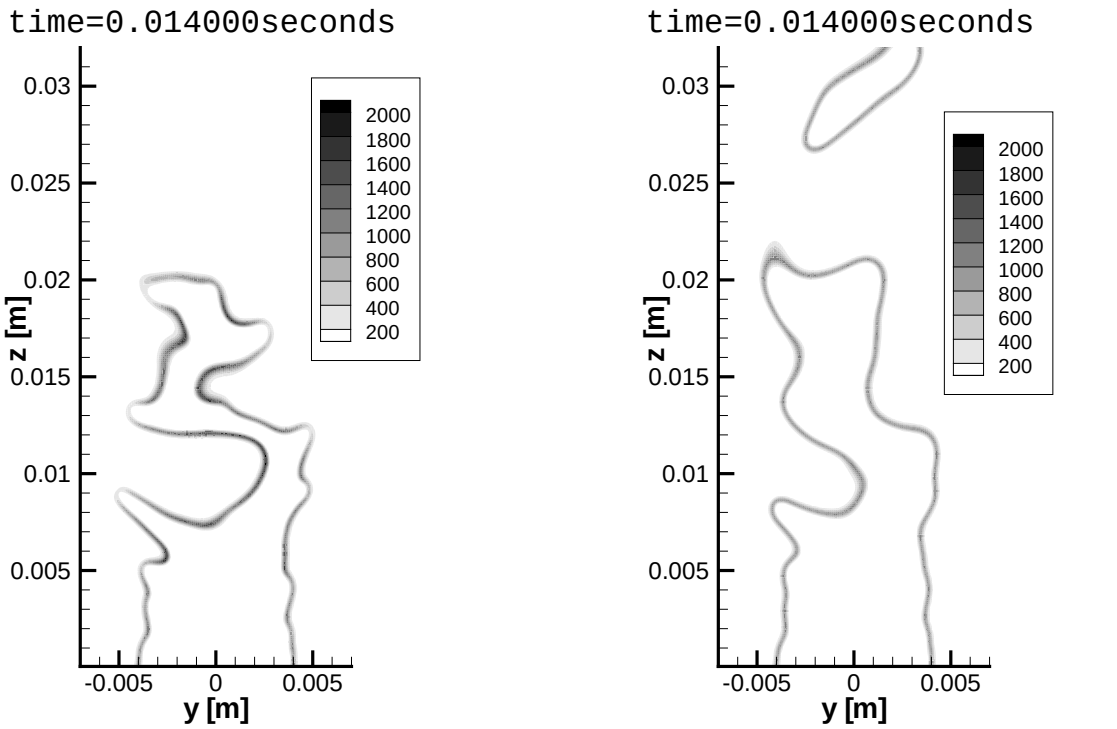

Figure 4: Contours of instantaneous ($t = 0.014$s) ω_c in the vertical plane $x_1 = 0$mm, for case A40 with 2D manifold (a) and B40 with 1D manifold (b).

Case	z_{tip} [mm]	s_T [m/s]	s_T/s_{L0}
A40	11.9	0.912	3.35
A40a	11.9	0.911	3.34
A40b	11.9	0.910	3.33
A40c	11.4	0.952	3.50
B40	15.9	0.698	2.56

Table 2: Overview of turbulent burning velocities s_T and locations of mean flame tip z_{tip} for the simulations with slot width 8mm. The laminar burning velocity s_{L0} equals 0.2724m/s for 40% H_2. See the previous table for descriptions of the different cases.

The effect of preferential diffusion is illustrated in Figs. 4-5. Each figure shows snapshots of the source term of the progress variable for the two simulations A40 and B40 in the same two-dimensional plane, Fig. 4 corresponding to $t = 0.0014$s and Fig. 5 to a slightly later time ($t = 0.0148$s). The difference between the two cases is remarkable. First, the maximum value of ω_c is twice as large when the two-dimensional manifold is used. Indeed the scatter plot shown in Fig. 2 confirms that regions with higher ω_c are accessed by simulation A40. This does not occur in case B40, since the one-dimensional manifold only allows (c, T) combinations that lie on the thick curve in Fig. 2. Fig. 4a shows that relatively high values of ω_c occur in regions convex toward the unburnt mixture, and relatively low values of ω_c (almost extinction) in regions concave toward the unburnt mixture. Thus the burning velocity of the convex parts is relatively large, while the burning velocity of the concave parts is relatively low. As a consequence the curvature becomes stronger, which would not happen if the burning velocity in convex and concave parts were the same (as in case B40). Therefore compared to B40, case A40 shows stronger spikes ejecting from the fuel and larger holes digged into the fuel. Simulations A40 and B40 show separate regions of unburnt fuel blown off by the tip of the flame (Figs. 4b and Fig. 5ab). Compared to case B40, the maximum height of the blown-off regions is much lower in case A40, and in case A40 it takes less time for such regions to burn completely.

The increase/decrease of burning velocity in convex/concave regions toward the unburnt mixture, which causes the relatively strong curvature in A40, is precisely what we would expect from the mechanism of preferential diffusion. Zeldovich (see Ref. [27]) argued that heat conduction smoothes out the curvature of the flame front, because concave parts give out more heat, thus lowering the burning velocity, and convex parts receive more heat, thus increasing the burning velocity. Diffusion of fuel has the opposite effect, provided the fuel is lean; diffusion of fuel enhances the curvature, because convex parts receive more fuel (ϕ and thus burning velocity increases when the fuel is lean) and concave parts lose more fuel (ϕ decreases). If the Lewis number of the fuel is smaller than one, the effect of diffusion of fuel is dominant over the effect of conduction of heat: the burning velocity is expected to increase in convex and decrease in concave regions.

Because of the stronger curvature we expect that the average height of the turbulent flame is reduced by preferential diffusion. This is indeed the case when we compare the locations of the mean flame tip for cases A40 and B40 (Table 2). It is obvious that compared to B40, the average height of A40 is much smaller, and as a consequence the turbulent burning velocity of A40 is significantly higher. The height of a jet flame is

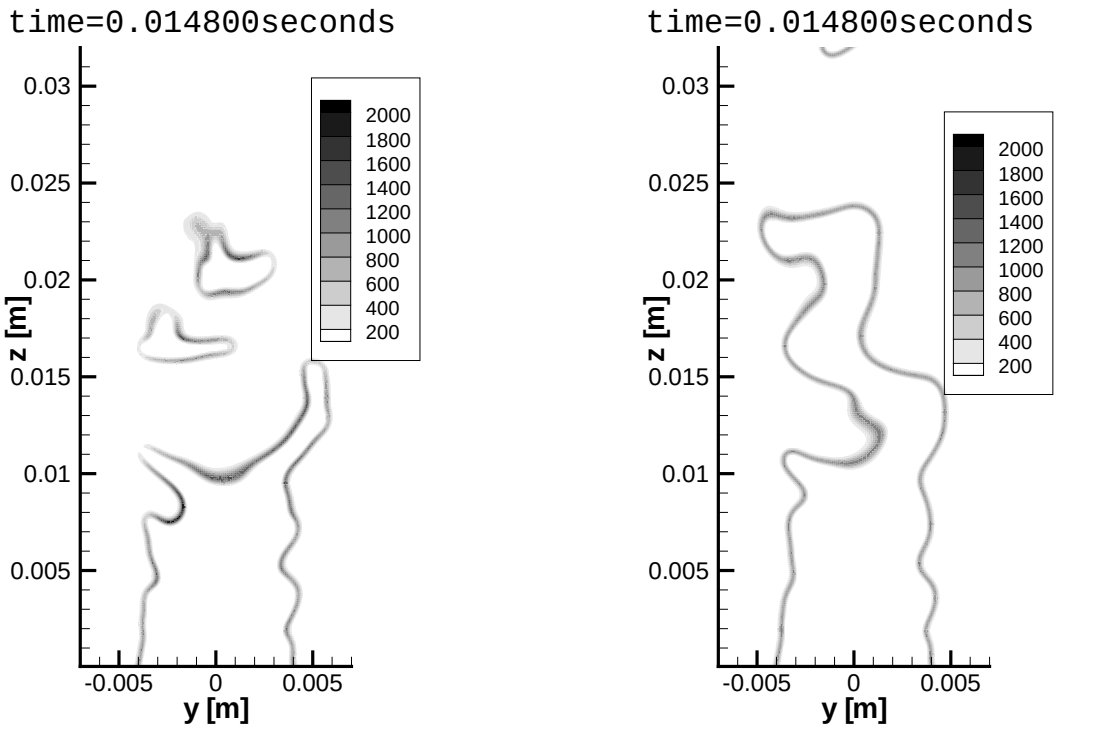

Figure 5: Contours of instantaneous ($t = 0.0148$s) ω_c in the vertical plane $x_1 = 0$mm, for case A40 with 2D manifold (a) and B40 with 1D manifold (b).

important in applications, such as gas-turbines, where addition of hydrogen to the fuel is a practical issue. If the flame shortens because of preferential diffusion, safety rules regarding the location of the flame tip, necessary to prevent flash-back of the flame into the burner, may be jeopardized.

The average flame tip z_{tip} represents the time average of the function $\tilde{z}_{tip}(t)$, which is defined as the minimum value of z for which the spanwise average of c at the centerline equals 0.5 at given time t. A turbulent burning velocity can be defined by [19]

$$s_T = \frac{u_0 L}{\sqrt{L^2 + z_{tip}^2}}, \tag{14}$$

where $L = 3.8$mm denotes the positive y-location at the inflow plane where $c = 0.5$. The basic flamelet burning velocity s_{L0} equals 0.2724m/s for 40% H_2 ($\phi = 0.7$).

Average flame tips and turbulent burning velocities have been summarized in Table 2. The most notable features, decrease of z_{tip} and increase of s_T when comparing case A40 to B40, were discussed above. Other effects quantified in the table are the effect of extrapolation beyond the outer flamelets and the role of the term ζ in the temperature equation. As indicated in section 2, two quite different procedures to extrapolate the manifold beyond the outer flamelets were applied. It turns out that the shape of the manifold outside the outer flamelets has negligible influence on the mean flame tip and turbulent burning velocity (compare A40 with A40a and A40b; another type of extrapolation was used in A40a, while in A40b the lower part of the manifold was extended down to $T_0 = 200$K, by adding 25 extra flamelets). Finally, the complicated term ζ, which roughly equals $-0.1\omega_T$, does influence the results. When this term is omitted from the temperature equation, z_{tip} decreases and s_T increases (compare A40c to A40). This is consistent with the fact that the manifold function $\zeta(c, T)$ is negative for most combinations (c, T).

5 Definition and results of simulation set II

In this section simulations with a smaller slot width are considered: 4 instead of 8mm. More specifically the T=1504K value at the inflow plane was located at $y = \pm 2$mm. The basic flamelet imposed at the inlet prescribed the value L where the progress variable under consideration equals 0.5. The slot width was reduced to enable simulations with lower turbulent burning velocities (tall flames, relative to the slot width). Thus the streamwise extent of the domain relative to the slot width could be increased when necessary. The inflow mean velocity, turbulent intensity and Kolmogorov scale just away from the inflow were approximately the same as in the previous section, while the length-scale and time scale of the inflow perturbation were halved, like the slot width.

Lower turbulent burning velocities are expected if we reduce the amount of hydrogen in the fuel, to 0% for example. It is interesting to compare such a case to the 40% hydrogen case to assess the effect of hydrogen addition on length and turbulent burning velocity of the flame. For 0% hydrogen the laminar burning velocity is smaller and preferential effects are less important, two reasons to expect a lower turbulent burning velocity.

For 0% hydrogen in the fuel, the stretch has a different effect upon the flame ($\Delta\phi/\Delta T_0 = -1.1 \times 10{-}3\,\mathrm{K}^{-1}$), which leads to crossing flamelets when the flamelets are drawn in a

plane with temperature on one of the axes. Therefore another second control variable had to be selected, for which the mass fraction of O_2 was chosen. Since the progress variable has to be monotonic, it is not possible to include hydrogen into the progress variable for the 0% hydrogen case. To represent the later stages of the reaction well for 0% hydrogen, a progress variable based upon the mass fraction of CH_4 solely is not very suitable, since that mass fraction does not cover the later stages of the reaction appropriately. Therefore it was decided to include the mass fraction of CO_2, which covers also the later stages of the reaction into the progress variable.

The simulations presented in this section are listed in Table 3. The first simulation, A40sT used the approach presented in the previous section (but here for the smaller slot width): progress variable based upon CH_4 and H_2, and second control variable T. However, the simulations denoted with 'sO' used the mass fraction of O_2 (Y_4) as second control variable instead of the temperature. Thus the temperature equation was omitted, T was obtained from the manifold, while we added the scalar equation for Y_4. The latter equation reads

$$\frac{\partial \rho Y_4}{\partial t} + \frac{\partial \rho u_j Y_4}{\partial x_j} = \frac{\partial}{\partial x_j}\Big(\frac{\rho D}{Le_4}\,\frac{\partial Y_4}{\partial x_j}\Big) + \omega_4, \tag{15}$$

where $Le_4 = 1.108$, while ω_4, the source term for the mass fraction of O_2, was obtained from the database.

Several manifolds co-spanned by O_2 were constructed, all using a progress variable c defined by

$$c = \frac{Y - Y_u}{Y_b - Y_u}, \tag{16}$$

$$Y = \frac{\alpha_5 Y_5}{M_5} - \frac{Y_1}{M_1} - \frac{\alpha_2 Y_2}{M_2}, \tag{17}$$

where Y_5, Y_1 and Y_2 denote the mass fraction of CO_2 (with Lewis number $Le_5 = 1.367$), CH_4 and H_2 respectively. In addition, subscripts b and u denote burnt and unburnt side of the flamelet, M_i represents the molar mass corresponding to Y_i, while the coefficients α_5 and α_2 have been specified in Table 3. We used $\alpha_5 = 1$, for all the manifolds co-spanned by O_2, but the value of α_2 was varied to investigate the influence of H_2 in the progress variable. The three last computations listed in Table 3, were performed with only one transport equation (for c). The manifold for each of these three cases reduced to the corresponding basic flamelet.

The diffusion flux in the equation of c, where c is defined by equation (16) is formally given by:

$$\frac{\partial}{\partial x_j}\Big[\frac{\rho D}{Y_b - Y_u}\Big(\frac{\alpha_5}{M_5 Le_5}\,\frac{\partial Y_5}{\partial x_j} - \frac{1}{M_1 Le_1}\,\frac{\partial Y_1}{\partial x_j} - \frac{\alpha_2}{M_2 Le_2}\,\frac{\partial Y_2}{\partial x_j}\Big)\Big]. \tag{18}$$

In the previous section we evaluated Y_1 and Y_2 in the analogous term from the manifold and subsequently performed the three-dimensional differentations. Unfortunately, this approach introduced numerical instabilities when a third mass fraction (CO_2) was included. Therefore we adopted an alternative method, which relies upon the plausible assumption that the variation of species in manifold space is mainly directed along the flamelet curves. Thus expression (18) can be approximated by

$$\frac{\partial}{\partial x_j}\Big[\frac{\rho D}{Le_c}\frac{\partial c}{\partial x_j}\Big], \tag{19}$$

Case	2nd control variable	H_2 in fuel	α_2	α_5	grid	h [1mm]	time step [10^{-6}s]
A40sT	T	40%	1	0	$80 \times 128 \times 160$	0.1	1.6
A40sO	O_2	40%	1	1	$80 \times 128 \times 320$	0.1	1.6
A40sOa	O_2	40%	0	1	$80 \times 128 \times 320$	0.1	1.6
A40sOb	O_2	40%	0.5	1	$80 \times 128 \times 320$	0.1	1.6
A40sOc	O_2	40%	2	1	$80 \times 128 \times 160$	0.1	0.8
A40sOd	O_2	40%	∞	0	$80 \times 128 \times 160$	0.1	0.8
A00sO	O_2	0%	0	1	$80 \times 128 \times 320$	0.1	1.6
B40sT	-	40%	1	0	$80 \times 128 \times 320$	0.1	1.6
B40sO	-	40%	1	1	$80 \times 128 \times 320$	0.1	1.6
B00sO	-	0%	0	1	$80 \times 128 \times 320$	0.1	1.6
C40sOa	O_2	40%	1	1	$40 \times 64 \times 80$	0.2	3.2
C40sOb	O_2	40%	1	1	$80 \times 128 \times 160$	0.1	1.6
C40sOc	O_2	40%	1	1	$160 \times 256 \times 320$	0.05	0.4

Table 3: Overview of simulations of turbulent Bunsen flame with slot width 4mm. The time step was determined by the diffusive stability restriction for c; no substeps for the scalar equations were used, except in cases A40sT and B40sT. Cases starting with 'B' used a single flamelet ($T_0 = 300$K), while the other simulations were based on 101 flamelets (200K$\leq T_0 \leq$400K).

where the temporally and spatially varying Lewis number Le_c is defined by

$$\frac{1}{Le_c} = \frac{\frac{\alpha_5}{M_5 Le_5}\frac{\partial Y_5}{\partial s} - \frac{1}{M_1 Le_1}\frac{\partial Y_1}{\partial s} - \frac{\alpha_2}{M_2 Le_2}\frac{\partial Y_2}{\partial s}}{(Y_b - Y_u)\frac{\partial c}{\partial s}}. \tag{20}$$

Here s is the spatial coordinate of the one-dimensional local flamelet; it can also be interpreted as the coordinate in the manifold space along the direction of the local flamelet in manifold space. Thus Le_c is a function of c and Y_4 only. It was precomputed and stored into the database, from which it was retrieved during the three-dimensional simulations, which applied expression (19).

Results for these simulations have been summarized in Table 4 ('sT' or 'sO' denote the second scalar, T or O_2 respectively). It appeared that the change of manifold (O_2 instead of T, adding CO_2 to progress variable) influenced the results to some extent; the turbulent burning velocities of A40sT and A40sO differed with about 11%. This discrepancy is further discussed below, together with additional simulations performed to exclude some possible causes.

Compared to the 'sT' run, the 'sO' run used a different treatment for the diffusion of c. However, this can not explain the differences; rerunning 'sT' with the Le_c altered the result less than 0.1%. Further, the discretization of the manifold space was found to be sufficiently accurate (200×200 for 'sT' and 500×500 for 'sO', errors were less than 0.5%; we repeated 'sT' for a manifold discretization of 500×500, and 'sO' with a manifold discretization of 1000×1000). For the 'sT' method the temporal resolution was verified by halving the time-step without substeps for the scalar equation, which reduced the

turbulent burning velocity with less than 1%. In addition the temporal and spatial resolution was verified by performing simulations on three different grids. These simulations are denoted by 'C' in table 3-4 and were performed at slightly higher inflow turbulence intensity (0.73m/s instead of 0.6m/s). Grid refinement with a factor of 2 in each spatial direction (and a time step reduction of a factor 4) showed a 0.7% increase of the turbulent burning velocity, while grid coarsening with a factor of 2 in each direction showed a 7% reduction. According to these numbers the convergence was second order at least. Thus we may deduce from these numbers that the numerical error on a mesh size of $h = 0.1$mm (compared to the solution on an infinitely fine mesh) was less than 1%. To explain this, we denote the unknown turbulent burning velocity as function of gridspacing with $s_T(h)$, and we assume a leading order convergence behavior of $s_T(h) = s_T(0) + ch^q$ where c and q are constants. Since we know the values $s_T(h)$, $s_T(2h)$ and $s_T(4h)$ ($h = 0.1$mm), we have three equations and three unknowns, such that we are able to compute $s_T(0)$; thus an error estimate smaller than 1% is obtained. The computational demand of grid refinement is too high to do it for all cases. Nevertheless, it is quite probable that the numerical errors were also less than 1% for the cases that used different manifolds, but the same grid.

Therefore, the difference between results of 'sT' and 'sO' should most likely be explained from the fact that the control variables of the manifold were not the same in both cases. Since, the change of control variable slightly altered the value of L, we should compare the values of the turbulent burning velocity, rather than the values for z_{tip}. Then it appears that for the single flamelet approach the choice for the progress variable hardly influences the result (compare the turbulent burning velocities of cases B40sT and B40sO). However, for two control variables the choice of control variables clearly matters. Another pair of control variables implies another pair of effective Lewis numbers in the 3D transport equations. Thus the choice of control variables influences the 3D preferential instability mechanism in the model and thereby the turbulent burning velocity.

Table 4 clearly shows that the presence of H_2 in the progress variable is essential to capture the effect of the preferential diffusion. This is also shown by the scatter plots in Fig. 6, where the first two plots correspond to cases A40sO (with H_2 in c) and A40sOa (no H_2 in c), respectively. Because of the presence of H_2, the Lewis number Le_c is considerably smaller than 1 in the first case, allowing the preferential diffusion mechanism to act in three dimensions. The scatter plot for the other progress variable shows a striking difference: since the Lewis number Le_c is much larger, the scatter points almost coincide with the basic flamelet. The turbulent burning velocity predicted by the simulation A40sOa, which used the two-dimensional manifold without hydrogen in c, was as high as the one obtained with the single flamelet (B40sO). These two simulations underpredicted the turbulent burning velocity with about 20%, compared to simulation A40sO.

Whereas it is essential to include H_2 into the progress variable, comparison between the cases with different α_2 indicate that the precise weight of H_2 in the progress variable is less important (see A40sO, A40sOb, A40sOc and A40sOd). Provided α_2 is nonzero, the variation of turbulent burning velocity obtained for different values of α_2 was relatively small. Similar results were obtained even for $\alpha_2 = \infty$, which required more computational cost due to the increased stiffness caused by the $\alpha_2 = \infty$ progress variable, which consisted entirely out of the species H_2.

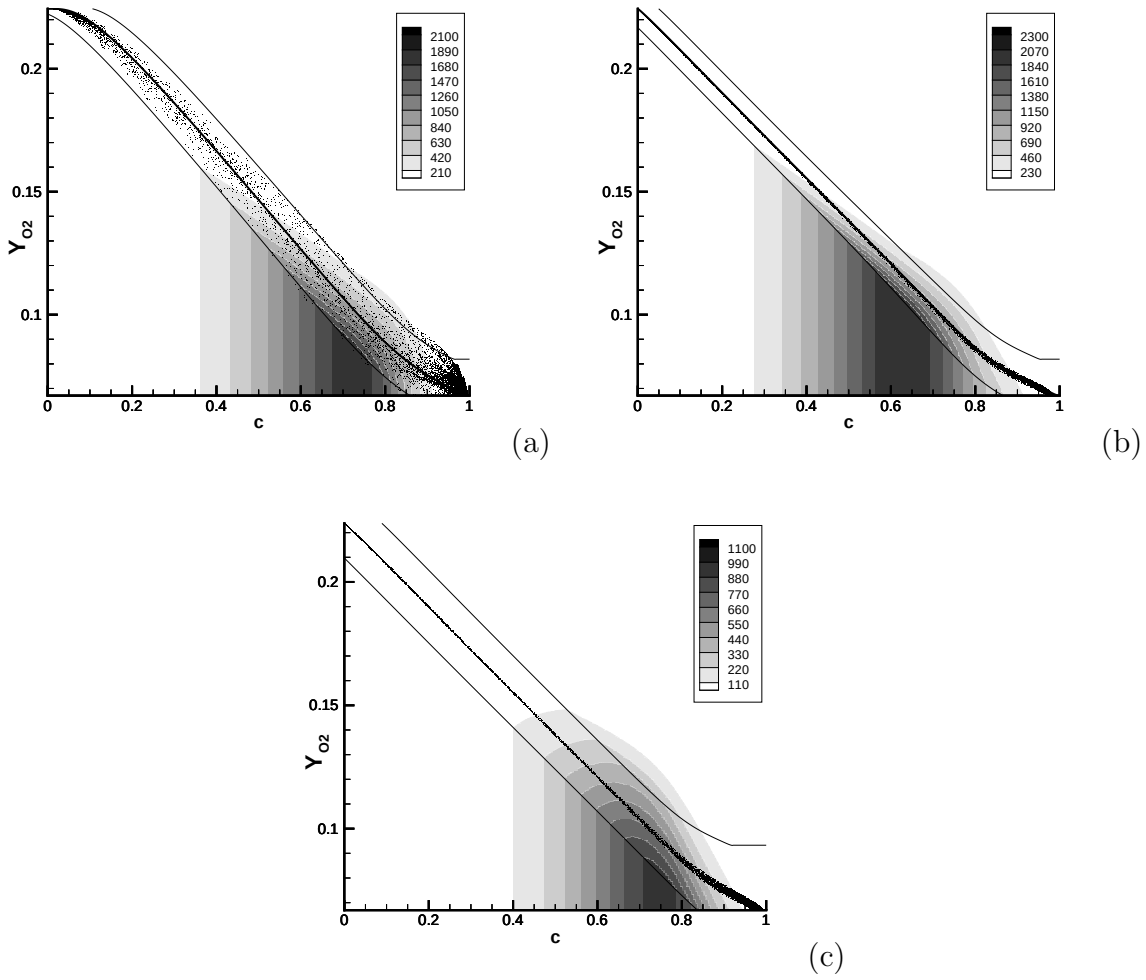

Figure 6: Scatter plots drawn on top of the manifolds for cases A40sO (a), A40sOa (b) and for A00sO (c). The gray shading denotes the contours of source term ω_c [kg/(m^{3}s)]. The thick solid curve corresponds to the basic flamelet ($\phi = 0.70$, $T_0 = 300$K). The upper thin solid curve represents the outer flamelet $T_0 = 200$K and the lower thin solid curve the outer flamelet $T_0 = 400$K. The scatter plots show actual (c, Y_4) combinations that were accessed by the corresponding simulations.

Case	L [mm]	z_{tip} [mm]	s_T [m/s]	s_T/s_{L0}
A40sT	1.770	7.72	0.670	2.46
A40sO	1.855	7.21	0.748	2.75
A40sOa	1.880	10.32	0.539	1.98
A40sOb	1.868	7.64	0.714	2.62
A40sOc	1.838	7.29	0.734	2.70
A40sOd	1.695	7.74	0.639	2.35
A00sO	1.851	13.00	0.423	2.19
B40sT	1.770	10.11	0.517	1.90
B40sO	1.855	10.66	0.515	1.89
B00sO	1.851	13.02	0.423	2.19
C40a	1.855	7.183	0.7515	2.76
C40b	1.855	6.645	0.8094	2.97
C40c	1.855	6.550	0.8137	2.99

Table 4: Overview of turbulent burning velocities s_T and locations of mean flame tip z_{tip} for the simulations with slot width 4mm. The laminar burning velocity s_{L0} equals 0.2724m/s for 40% H_2 and 0.1929m/s for 0% H_2. See the previous table for descriptions of the different cases.

Figure 6c shows the scatter plot for the 0% hydrogen case (A00sO), whose scatter points were very near to the basic flamelet (like in case A40sOa). This means that a single flamelet is sufficient to perform a simulation for 0% hydrogen; for 0% hydrogen and present turbulent activity it is apparently not necessary to include stretch effects in the flamelet generated manifold. Indeed the simulation with a single flamelet (B00sO) produced results quite similar to those of the simulation with the two-dimensional manifold (A00sO). Compared to 0% hydrogen, the turbulent burning velocity in case of 40% hydrogen was approximately 80% higher, provided 3D preferential diffusion was incorporated (the turbulent burning velocity of A40sO divided by the one of A00sO gives 1.8). When 3D preferential diffusion was omitted, we found an increase of 30% only (the turbulent burning velocity of A40sOa divided by the one of A00sO gives 1.3). The latter increase is somewhat less than the ratio of laminar burning velocities (equal to 1.4) suggests.

6 Conclusions

Direct numerical simulations of a lean premixed turbulent Bunsen flame with hydrogen addition were performed for two slot widths, 8mm in simulation set I, and 4 mm in set II. We focussed on a premixed fuel with equivalence ratio 0.7 and a molar fractional distribution of 40% H_2 and 60% CH_4. The flamelet generated manifold technique was used to reduce the chemistry; flamelets with different equivalence ratio and inflow temperature were used to account for stretch effects induced by preferential diffusion. Three transport equations were solved in three dimensions, one for the progress variable, another for the temperature (set I) or oxygen (set II), and a third equation for NO, which was a passive

transport equation. The progress variable was based upon the molar fractions of CH_4 and H_2 in case of set I, and a third species (CO_2) was added for the simulations in set II. Appropriate nontrivial expressions were used for the diffusion of the progress variable. To validate the accuracy of the numerical discretization schemes, grid refinement was performed for one representative case in set II.

The simulation clearly showed an enhanced reaction rate in regions convex toward the reactants and reduced reaction rate in regions convex toward the products. Extinction occurred occasionally in the latter regions. The effect of preferential diffusion was quantified by comparison with a simulation in which a standard flamelet technique, based on a single variable, was used. Thus the standard technique did not incorporate preferential diffusion effects in the three-dimensional tranports equations, although the flamelet was obviously calculated using the appropriate Lewis numbers in one dimension. The comparison showed that inclusion of a second independent variable into the manifold was quite important, otherwise effects of preferential diffusion were not captured in the flame. Effects of preferential diffusion were shown to enhance curvature, and thereby to increase the turbulent burning velocity and reduce the mean flame height considerably.

Additional simulations in set I were included to address several issues, for example the validation of choices of extrapolation outside flamelet bounds. Also a simulation was performed to investigate the influence of the term that contains the species fluxes in the temperature equation. The term was found to be responsible for a reduction of the turbulent burning velocity of about 5%.

Simulation set II was included to investigate the role of the precise definition of the progress variable and to quantify the differences with 0% hydrogen addition. Since for these variations a larger ratio of flame height to slot width was expected, the slot width was reduced in set II to limit the computational costs. These simulations showed that it is mandatory to include hydrogen into the progress variable to capture the three-dimensional preferential diffusion mechanism, but that the precise value of the weight factor of H_2 is less important. Compared to 0% hydrogen, the case of 40% hydrogen increased the burning velocity with approximately 80%. When 3D preferential diffusion was ignored an increase of only 30%, primarily due to the increase of laminar burning velocity, was found.

Acknowledgement
This research was funded by Stichting Technische Wetenschappen, grant number EWO.5874.

References

[1] Chen, Y-C., Bilger, R.W. (2004) Experimental investigation of three-dimensional flame-front structure in premixed turbulent combustion II. Lean hydrogen/air Bunsen flames, Combust. Flame 138, 155-174.

[2] Bell, J.B., Cheng, R.K., Day, M.S., Shepherd, I.G. (2007) Numerical simulation of Lewis number effects on lean premixed turbulent flames, Proc. Combust. Inst. 31, 1309-1317.

[3] Bastiaans, R.J.M., Vreman, A.W., Pitsch, H. (2007) DNS of lean hydrogen combustion with flamelet-generated manifolds, CTR Annual Research Briefs 2007.

[4] Liu, C., Karim, G. (2008) A simulation of the combustion of hydrogen in HCCI engines using a 3D model with detailed chemical kinetics. Int. J. Hydrogen Energy 33, 3863-3875.

[5] Knop, V. Benkenida, A., Jay, S. Colin. O. (2008) Modelling of combustion and nitrogen oxide formation in hydrogen-fuelled internal combustion engines within a 3D CFD code. Int. J. Hydrogen Energy 33, 5083-5907.

[6] Schefer, R.W., Wicksall, D.M., Agrawal, A.J. (2003) Combustion of hydrogen-enriched methane in a lean premixed swirl-stabilized burner, Combust. Inst. 29, 843-851.

[7] Cozzi, F., Coghe, A. (2006) Behavior of hydrogen-enriched non-premixed swirled natural gas flames, Int. J. Hydrogen Energy 31, 669-677.

[8] Mandilas, C., Ormsby, M.P., Sheppard, C.G.W., Woolley, R. (2007) Effects of hydrogen addition on laminar and turbulent premixed methane and iso-octane-air flames, Proc. Combust. Inst. 31, 1443-1450.

[9] Halter, F., Chauveau, C., Gökalp, I. (2007) Characterization of the effects of hydrogen addition in premixed methane/air flames. Int. J. Hydrogen Energy 32, 2585-2592.

[10] Hawkes, E.R., Chen, J.H. (2004) Direct numerical simulation of hydrogen-enriched lean premixed methane-air flames, Combust. Flame 138, 242-258.

[11] Halter, F., Chauveau, C., Djebaili-Chaumeix, N., Gokalp, I. (2005) Characterization of the effects of pressure and hydrogen concentration on laminar burning velocities of methane-hydrogen-air mixtures, Proc. Combust. Inst. 30, 201-208.

[12] Ilbas, M. Crayford, A.P., Yilmaz, I., Bowen, P.J., Syred, N. (2006) Laminar-burning velocities of hydrogen-air and hydrogen-methane-air mixtures: An experimental study, Int. J. Hydrogen Energy 31, 1768-1779.

[13] Di Sarli, V., Di Benedetto, A. (2007) Laminar burning velocity of hydrogen-methane/air premixed flames, Int. J. Hydrogen Energy 32, 637-646.

[14] De Goey, L.P.H., Hermanns, R.T.E., Bastiaans, R.J.M. (2007) Analysis of the asymptotic structure of stoichiometric premixed CH4-H2-air flames, Proc. Combust. Inst. 31(1), 1031-1038.

[15] Hermanns, R.T.E. (2007) Laminar burning velocities of methane-hydrogen-air mixtures, PhD. Thesis, Eindhoven University of Technology, The Netherlands.

[16] Miao, H., Jiao, Q., Huang, Z. Jiang, D. (2008) Effect of initial pressure on laminar combustion characteristics of hydrogen enriched natural gas. Int. J. Hydrogen Energy 33, 3876-3883.

[17] Filatyev, S.A., Driscoll, J.F., Carter, C.D., Donbar J.M. Measured properties of turbulent premixed flames for model assessment, including burning velocities, stretch rates, and surface densities, Comb. Flame **141**, 1-21 (2005).

[18] Bell, J.B., Day, M.S., Grcar, J.F., Lijewski, M.J., Driscoll, J.F., Filatyev, S.A.: Numerical simulation of a laboratory-scale turbulent slot flame. Proc. Comb. Inst. **31**, 1299-1307 (2007).

[19] Sankaran, R., Hawkes, E.R., Chen, J.H., Lu, T., Law, C.K.: Structure of a spatially developing turbulent lean methane-air Bunsen flame. Proc. Comb. Inst. **31**, 1291-1298 (2007).

[20] Peters, N.: Turbulent Combustion, Cambridge University Press (2000).

[21] Vreman, A.W., van Oijen, J.A., de Goey, L.P.H., Bastiaans, R.J.M. (2009) Large-eddy simulation of turbulent combustion using premixed flamelet chemistry, accepted by Flow, Turb. Combust.

[22] Vreman, A.W., Bastiaans, R.J.M., Geurts, B.J. (2009) Accuracy of large-eddy simulation of premixed turbulent combustion, accepted by Flow, Turb. Combust.

[23] Bradley, D., Kwa, L.K., Lau, A.K.C., Missaghi, M. (1988) Laminar flamelet modeling of recirculating premixed methane and propane-air combustion, Combust. Flame 71, 109-122.

[24] Van Oijen, J.A., De Goey, L.P.H.: Modelling of premixed laminar flames using flamelet-generated manifolds. Combust. Sci. and Tech. **161**, 113-137 (2000).

[25] Gicquel, O., Darabiha, N., Thevénin, D.: Laminar premixed hydrogen/air counterflow flame simulations using flame prolongation of ILDM with differential diffustion. Proc. Combust. Inst. **28**, 1901-1908 (2000).

[26] Smith, G.P., Golden, D.M., Frenklach, M., Moriarty, N.W., Eiteneer, B., Goldenberg, M., Bowman, C.T., Hanson, R.K., Song, S., Gardiner, Jr., W.C., Lissianski, V.V., and Qin, Z. (1999) GRI-MECH 3.0, http://www.me.berkeley.edu/gri_mech/

[27] Shivashinsky, G.I. (1983) Instabilities, pattern formation, and turbulence in flames, Annu. Rev. Fluid Mech. 15, 179-199.

[28] Van Oijen, J.A. (2002) Flamelet-generated manifolds: development and application to premixed laminar flames. PhD. Thesis, TU Eindhoven.

[29] De Goey, L.P.H., Ten Thije Boonkkamp, J.H.M. (1999) A Flamelet Description of Premixed Laminar Flames and the Relation with Flame Stretch. Combust. Flame 119, 253–271.

[30] Van Oijen, J.A., de Goey, L.P.H. (2002) Modelling of premixed counterflow flames using the flamelet-generated manifold method. Combust. Theory Modelling 6, 463–478.

[31] Van Oijen, J.A. (2008) Preferential diffusion effects in stretched premixed methane-hydrogen-air flames. submitted to Combust. Theory Modelling.

[32] Smooke, M.D., Giovangigli, V.: Formulation of the premixed and nonpremixed test problems. In 'Reduced kinetic mechanisms and asymptotic approximations for methane-air flames', ed. M.D. Smooke, Springer Verlag Berlin, 1-28 (1991).

[33] Vreman, A.W., Albrecht, B.A., van Oijen, J.A., de Goey, L.P.H., Bastiaans, R.J.M. (2008) Premixed and non-premixed flamelet generated manifolds in large-eddy simulation of Sandia Flame D and F. Combust. Flame 153, 394-416.